Various types of defects detection in flat and curved laminated composite plates using nonintrusive Lamb wave system

Lingyu Yu
Department of Mechanical Engineering, University of South Carolina
300 Main Street, Columbia, SC, 29208; USA
yu3@ces.sc.edu
ASME Membership

Zhaoyun Ma[1]
Department of Mechanical Engineering, University of South Carolina
300 Main Street, Columbia, SC, 29208; USA
zhaoyun@email.sc.edu
ASME Membership

Abstract: Composite materials are widely used in aerospace industries due to their light weight, strength, and various other desired properties. However, they are susceptible to various defects occurring during the manufacturing process or in service. Typical defects include porosity, wrinkles, and delamination. Nondestructive means of detection of the defects at any stage are of great importance to ensure quality and safety of composite structures. A nonintrusive removeable Lamb wave system and accompanied methodology that is not material-dependent is presented in this paper to detect various types of typical defects in laminated composite plates, flat or curved. Through multidimensional data acquisition and processing, abnormality in waves caused by defects is captured and presented in inspection images. The methodologies are demonstrated in 2 cases: flat plate with wrinkles, and curved plate with delamination. Overall the results show that Lamb waves using the piezoelectric transducer and laser vibrometer system can be used for various types of defects inspection in flat or curved composite plates.

Keywords: composite structures, wrinkles, delamination, curvature, Lamb waves, Laser vibrometer

1. INTRODUCTION

Composite materials are widely used in aerospace and aeronautical industries, and the interest of using more advanced composites is growing high [1] because of their advantages for light weight, high strength, and engineering design flexibility. The large use of composites necessitates the development of appropriate nondestructive evaluation (NDE) methods to detect and quantify defects and damage in composites [2, 3]. The National Aeronautics and Space Administration (NASA) Aeronautics Research Mission Directorate initiated research to reduce the certification time of composite components under the Advanced Composites Project [3, 4] with one of the three technical challenges being developing NDE methods to quantitatively characterize defects in as-manufactured parts and damage incurred during or after manufacturing [2]. Various defects such as fiber waviness or undesirable material may appear in composite structures during the manufacturing process [5]. Wrinkles or waviness are common when adding new layers [6] or during curing with temperature gradients [2]. Wrinkles/waviness can be in-plane or out-of-plane [7] and will cause significant degradation of the composite strength and can weaken the composite structure performance. Debonding occurs when an adhesive stop adhering to an adherend or if physical or mechanical forces that hold the bond together are broken while delamination is a failure in a laminate which leads to separation of the layers or plies. All these undesirable defects affect the mechanical properties and structural overall performance [5], and may further jeopardize the safety of space structures during operation. Thus nondestructive evaluation methods that are suitable for a wide range of defects are highly needed [1, 8] for ensuring safety and reliability of aeronautic vehicles [4, 9].

Lamb waves can propagate relatively long distance in plate-like structures with lower energy loss compared to bulk waves, which enables their ability for large area inspection [10, 11], and they are sensitive to various defects [12, 13].

[1] Correspondence author.
E-mail address: zhaoyun@email.sc.edu (Z. Ma)

With these advantages, Lamb wave based NDE methods have been widely applied for defect detection in plate-like composite structures over the last decade [14-18]. Park et al. adopted time reversal algorithms to reconstruct the Lamb waves excited by a piezoelectric patch in a quasi-isotropic composite plate towards a reference free diagnosis technique [14]. Purekar and Pines used piezoelectric sensor (PZT) arrays to excite and receive Lamb waves for damage detection purpose in a composite plate with simulated delamination [15]. Rogge and Leckey demonstrated Lamb wavefield analysis and wavenumber imaging can be used to identify the depth and size of near surface impact delamination in composite plates [16]. Hall and Michaels studied multipath guided wave imaging method using sparser arrays on a composite plate with simulated damage, resulting in improved image quality compared to their previous work [17]. Sohn et al. applied a filtering imaging method and highlighted the internal delamination using standing waves trapped within on a composite plate [18]. Tian et al. quantified impact delamination dimensions in composite plates through wavenumber based imaging methods [19].

Recently, the scanning laser Doppler vibrometer (SLDV) has attracted great interests for Lamb wave based defect detection, visualization, and quantification [13, 20-24]. Based on the Doppler effect, the SLDV can acquire velocities/displacements of Lamb waves on the plate surface where the laser inspection spot aims at. By scanning over a high-density set of points over the wave propagation area, the SLDV can acquire a high-resolution wavefield, which contains a wealth of information about the Lamb wave propagation and interactions with defect in plates. Such high-resolution wavefields have been used for visualization and quantification of various types of defects, such as cracks, delamination, and debonding [25-29]. However, most of the work reported in literature for Lamb wave based defect detection in composites is mainly about delamination on flat plates [9].

This paper investigates the detection and evaluation of wrinkles and delamination defects either in flat or curved laminated composite plates using PZT-SLDV Lamb waves and multidimensional wavefield analysis. Laboratory experiments are first set up to provide minimally invasion to the plates being inspected and the Lamb wave wavefields are obtained. For defect visualization and evaluation, two methods, adaptive wavefield imaging and wavenumber imaging, are developed and applied for the flat and curved plate scenarios respectively. The inspection results show that the imaging methods not only visually show the location of the defects, but can also roughly quantify their sizes. The remainder of this paper is organized as follows: Section 2 presents the nonintrusive PZT-SLDV inspection experimental setup. Section 3 presents the visualization and localization of wrinkle defects in a flat composite plate, while Section 4 presents that in a curved plate with delamination. Section 5 then concludes the paper with findings, discussions, and future work.

2. NONINTRUSIVE PZT-SLDV LAMB WAVE SYSTEM SET UP

This section presents the nonintrusive experimental setup of the PZT-SLDV Lamb wave inspection system. The overall experimental setup of the PZT-SLDV system is given in Figure 1. A Steminc SM412[1] PZT transducer (0.5 mm thick and 7 mm diameter) is used for Lamb wave actuation, while the Polytech PSV-400-M2 SLDV system is employed for wavefield sensing. Traditionally, the PZT transducer is bonded on the surface with permanent adhesive as couplant, while reflective tapes are attached on the specimen surface for SLDV signal enhancement [22]. Removing the PZT transducer or the reflective tape requires great care and may more or less still cause adversely modification of the material surface conditions. In order to implement truly nondestructive evaluation on the composite structures, nonintrusive setup is explored and implemented in this study, with selected honey (Figure 2a) (Simply Balanced from market[2]) as couplant for PZT actuation and wipe-off reflective spray (Figure 2b) (Albedo 100 reflective spray[3]) for SLDV measurement enhancement.

To attach the PZT transducer, a syringe is used to apply a tiny drop of honey at the target surface and the PZT is then placed on top of the honey drop. Gentle thumb pressure is applied on the PZT transducer for about two minutes so that the honey will distribute evenly between PZT and the specimen. The attached PZT is then left for a couple of hours before inspection so that the honey will be harden and cure. Figure 2c illustrates the PZT transducer attached on the surface with honey. Removable transparent tape is used to hold the wire in place on the plate (as shown in Figure 2c) to help the PZT stay on without sliding down if the specimen is placed vertically. On the other hand, the wipe-off reflective spray is applied with the spray nozzle being held 12 inches away and normal to the specimen

[1]https://www.steminc.com/PZT/en/
[2]https://www.target.com/p/organic-honey-16oz-simply-balanced-8482/-/A-53385493
[3]https://www.amazon.com/gp/product/B00WRNPI50/ref=ppx_yo_dt_b_search_asin_title?ie=UTF8&psc=1

surface as shown in Figure 2d. About 20 layers of spray is applied to the surface in order to achieve full signal level from the SLDV.

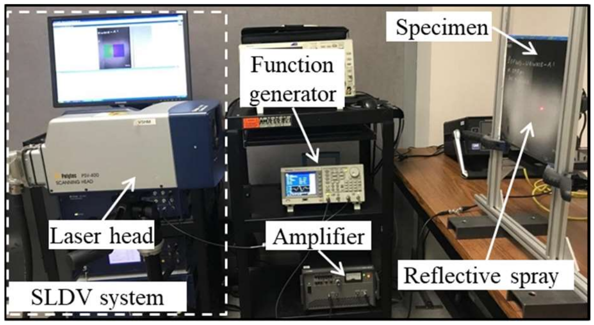

Figure 1 Experimental setup of the non-intrusive PZT-SLDV system

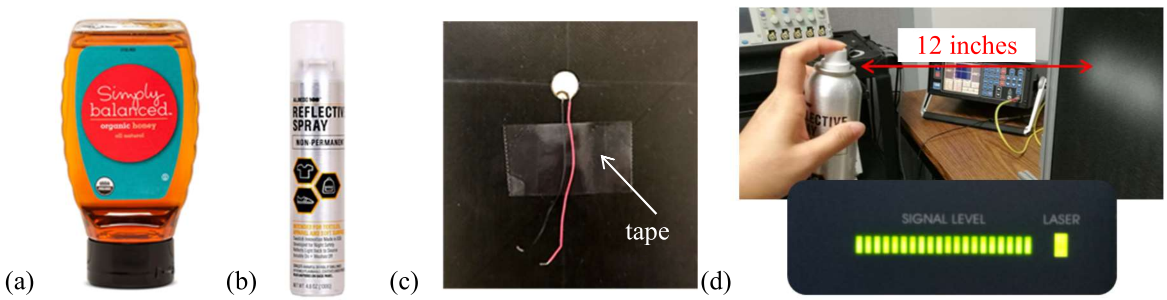

Figure 2 Non-intrusive PZT-SLDV system setup: (a) Honey couplant by Simply Balanced, (b) wipe off reflective spray by Albedo 100, (c) PZT attached using honey as couplant. Transparent tape is used to hold the wire in place on the plate. and (d) spray applying illustration and related signal strength

For Lamb wave inspection, 3-count Hanning window smoothed sinusoidal is used as excitation. It is generated by a function generator (Tektronix AFG3022C) at a selected frequency, magnified by an amplifier (NF HSA 4014), and then sent to the PZT actuator. Through in-plane piezoelectric coupling [10], Lamb waves are excited and propagate in the plates. On the sensing side, SLDV works on the Doppler frequency-shift effect on light waves and measures particle velocity along its laser beam. For Lamb wave measurements, the SLDV head is placed normal to the specimen to obtain the out-of-plane Lamb wave velocity at a sensing point. With its scanning capability, SLDV will obtain the motions over a user defined scanning line or area grids and output the multidimensional time-space Lamb wavefield $v(t,\mathbf{x})$, where t is the time and $\mathbf{x}$ is the space vector (x,y) of the scanning point. More details of SLDV wavefield sensing can be found in [19].

3. WRINKLES INSPECTION ON A FLAT PLATE

In this section, a flat laminated composite plate with out of plane wrinkle defects is inspected. Within the acquired multidimensional time-space wavefield wave-wrinkle interactions are observed. An adaptive wavefield imaging method has been developed using the time of flight information of the first arrival in the acquired waves and applied to evaluate the wrinkle defect.

3.1. EVALUATION METHOD: ADAPTIVE WAVEFIELD IMAGING

Very often, directly acquired wavefield does immediately show the wave-defect interactions, indicating the existence of structural discontinuity [18, 19, 29, 30]. However, such detection requires experiences of wavefield analysis and immediate visualization of discontinuity in the structure is highly desired. Studies have shown that evaluating the wave energy along the wave propagating distance provides a rapid yet effective way to generate an inspection image of the plate [31, 32]. The wave energy can be represented by quantities such as the peak amplitude or the root-meansquare value of the waveform at the position [33]. However, it has shown that the resolution of such images are limited and the revealed defect features are not clear enough for quantification purpose [33].

Due to the multimodal property of Lamb wave [34] there are always at least two modes existing in the propagation. They usually travel at largely different velocities, resulting in a faster wave packet arriving first than other slower ones. The first arrival will yield clearer interaction features since it is less likely complicated by the slower modes or boundary reflections [33]. In this research, an adaptive wavefield imaging method has been developed that employs the first arrival for the evaluation of wrinkle defects in the flat composite panel. Assume the group velocity c_g of such a first arrival is known, its time of flight at a point (x,y) of interest in the plate can be determined as:

$$t_{tof}(\mathbf{x}) = \frac{\left|\sqrt{(x-x_0)^2+(y-y_0)^2}\right|}{c_g} \tag{1}$$

where (x_0,y_0) is the location of excitation source. Using the calculated $t_{tof}(\mathbf{x})$, the first arrival of the acquired wave can be retained through a windowing technique. The window $W_{t_{tof}}(t)$ is defined with its center at $t_{tof}(\mathbf{x})$ and having a width of double length of the excitation signal. The window is then applied to the wavefield as:

$$v_{1\mathrm{st}}(t,\mathbf{x}) = v(t,\mathbf{x})W_{tof}(t) \tag{2}$$

In our work, a Tukey window [35] is used since it offers a "flat top" to offer unit gain within the interested time frame of first arrival signals. Using the windowed first arrival, an intensity image based on the amplitude information is then generated to indicate the presence of the defect as well as its locationas:

$$v_{1\mathrm{st}}^{mag}(t,\mathbf{x}) = \max\left|v_{1\mathrm{st}}(t,\mathbf{x})\right| \tag{3}$$

3.2. EVALUATION OF WRINKLE DEFECT

The flat composite plate is manufactured with total 20 plies and 3.83 mm thickness. The overall dimension of the plate is measured at 306 × 260 (unit: mm). Significant wrinkles can be observed on both top and bottom surfaces, as illustrated in Figure 3a (indicated by the arrows), and also can be seen from the side along the thickness direction as in Figure 3b. No other information of this wrinkle plate is available such as the material properties as well as the detailed layup. To assist the inspection, Cartesian coordinates are employed with the origin set at the left bottom corner of the plate. We have chosen to study the area with more visible wrinkles and referred it as "wrinkle region", in contrast to the area with less visible wrinkles as "reference region", as shown in Figure 3c. A PZT actuator is placed at location (160, 110) on the specimen (Figure 3c) to excite the waves. Area scans (95 mm by 60 mm) are performed on both the top and bottom surfaces in the wrinkle region, using the area scan setup given in Figure 3c. Line scan within the reference area has also been performed for inspection parameter setup. The SLDV scanning spatial resolution is 1 mm and the sampling rate is 10.24 MHz.

For Lamb waves NDE, as frequencies go higher, more wave modes are likely to be excited and cause complexity in subsequent damage evaluation. Therefore, low frequency is often employed [36]. Two quick wave acquisition through line scans (Figure 3c) to identify a proper excitation frequency are first performed in the reference region. The scans are along x axis from 10 to 100 mm away from the PZT actuator at 120 kHz and 210 kHz. The acquired time-space wavefield as well as a waveform at a certain propagating distance are presented in Figure 4 for both frequencies. From Figure 4a, we can see that there are two wave packets in the 120 kHz Lamb waves but the first arrival at about 30 µs has very weak strength. On the other side, the first arrival of the waves at 210 kHz in Figure 4b exhibits much stronger strength and will be ideal for the wrinkle inspection since we are set to use the first arrival as stated in section 3.1. Thus, 210 kHz will be used as the excitation frequency for the inspection in the wrinkle plates.

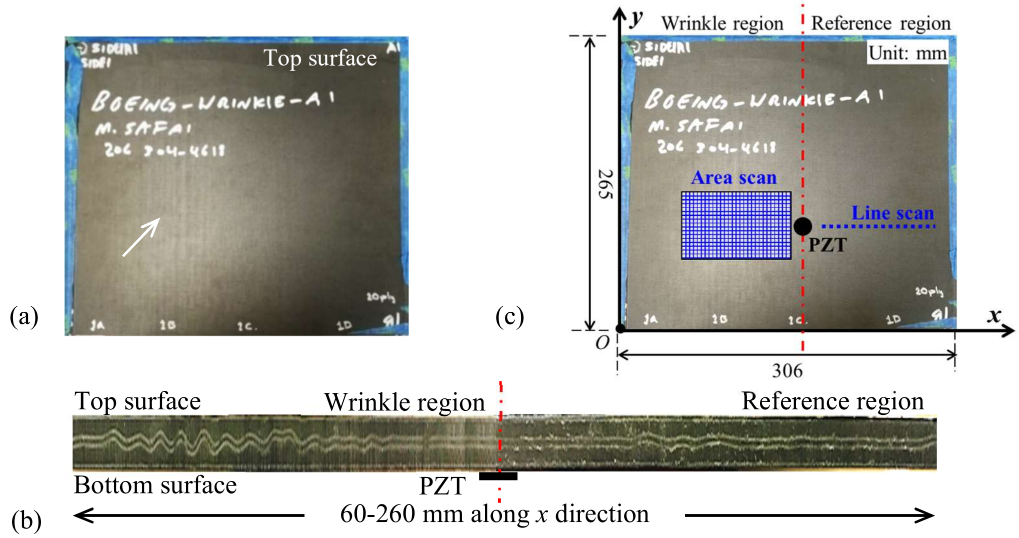

Figure 3 Inspection of composite plate with wrinkle defect (photo courtesy of NASA Langley Research Center and Boeing): (a) top surface, (b) side view, and (c) actuation and sensing schematic

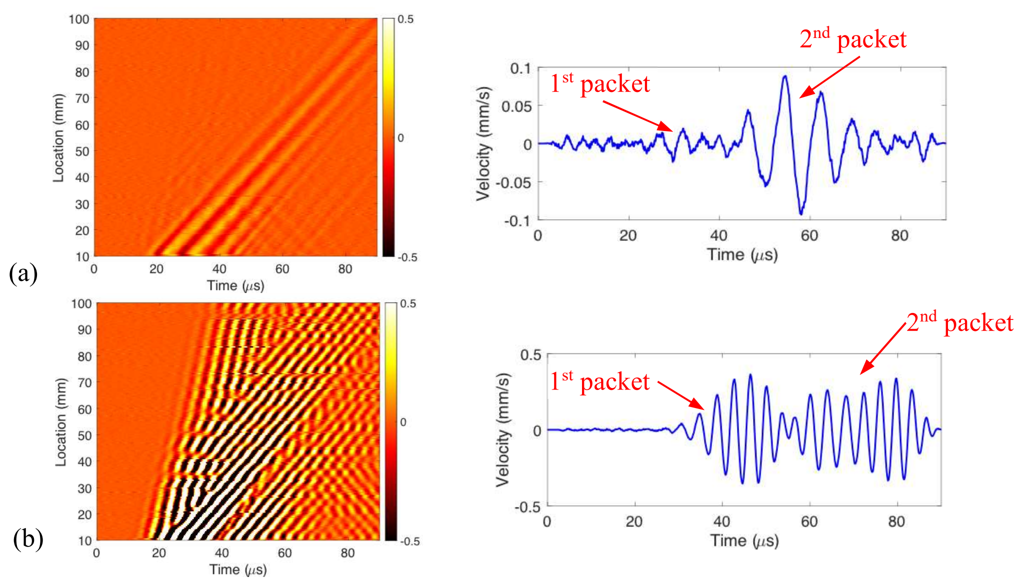

Figure 4 Line inspection results: (a) time-space wavefield at 120 kHz, and representative waveform at 50 mm, (b) time-space wavefield at 210 kHz, and representative waveform at 85 mm

To implement the imaging algorithm, the group velocity of the first arrival in the acquired waves at 210 kHz needs to be determined by finding out its time of flight (TOF) at a given propagation distance. To estimate the group velocity more accurately, eleven signals from 70 to 90 mm at a 2 mm increment along the scanning line are used. Three example waveforms at propagating distance 70, 80, and 90 mm are plotted in Figure 5a. Hilbert transform is applied to extract the envelops of these waveforms and the TOFs of the first arrivals are extracted indicated by the peak arrival time (e.g. TOF is 47.5 μs at 90 mm in Figure 5a). All of the acquired TOF and corresponding propagating distance are plotted in Figure 5b (blue stars). The plot shows a linear relationship which can be curved fitted through linear regression (red line, derived with linear curve fitting as $y = 5.249x - 158.23$). The group velocity of the first arrival is therefore obtained, which is about 5.249 mm/μs.

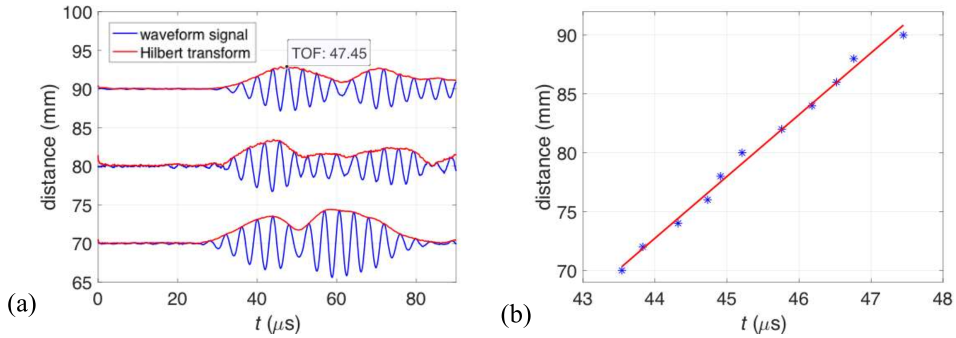

Figure 5 Group velocity estimation of the first arrival: (a) waterfall plots of representative waveforms (at propagating distance 70, 80, and 90 mm) that are used for the group velocity estimation, and (b) more accurate group velocity estimated by the slope of linear regression results

Inspection using the subject PZT-SLDV system is performed on the wrinkle region on both top and bottom surfaces of the test plate using the setup given in Figure 3c. The resulted time-space wavefields are presented in Figure 6. Circular wavefront can be observed in the incident waves leaving the PZT actuator for both results. The circular wavefronts then changed to straight crest ones when they arrived at and passed through the wrinkles. Comparing the waves measured on the top (Figure 6a) and bottom (Figure 6a), the wave interaction with defects are occurring in similar range (90 to 130 mm along *x* direction). It matches with the visually observed wrinkle range in the plate. The detection of wrinkles from both top and bottom indicates the wrinkles might be manufactured through the thickness and can be inspected from either side.

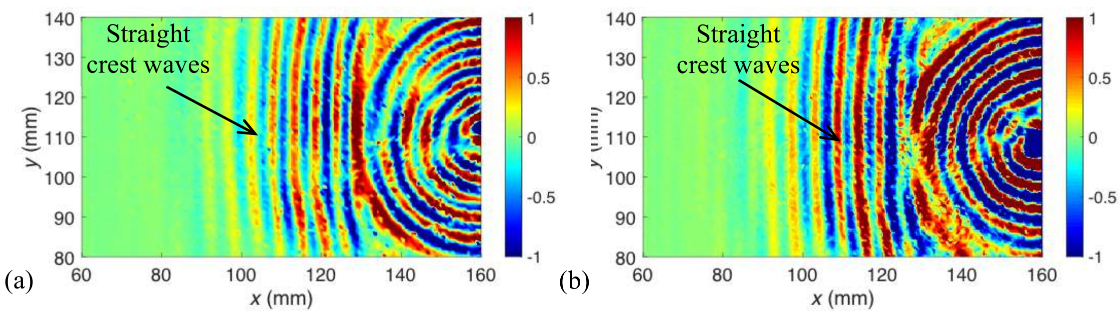

Figure 6 Wavefield results at 29 µs of the wrinkle region measured on: (a) top surface, and (b) bottom surface, both showing incident circular crest waves change to straight crest waves when

The wavefield data have been further processed with the adaptive wavefield imaging method outlined in section 3.1 and the results are given in Figure 7a and Figure 7c for top and bottom surface respectively. It can be observed that the wave energy has two distinguish distributions in the range 80 to 130 mm and 130 to 160 mm in both images. In the range 130 to 160 mm, the strong energy from the incident waves are observed with a circular shape. While in the range 80 to 130 mm, strip shaped wave energy distribution is observed. The zoom in images of the wrinkle range are presented in Figure 7b and Figure 7d for top and bottom surface respectively. Clear wrinkle patterns are visualized now with peak and valleys represented by the blue and red color in both images. The wrinkle patterns are discernibly visualized in both images within the range 80-130 mm along *x* direction, and the identified wrinkle ranges agree well with that observed through visual examination given in Figure 3b.

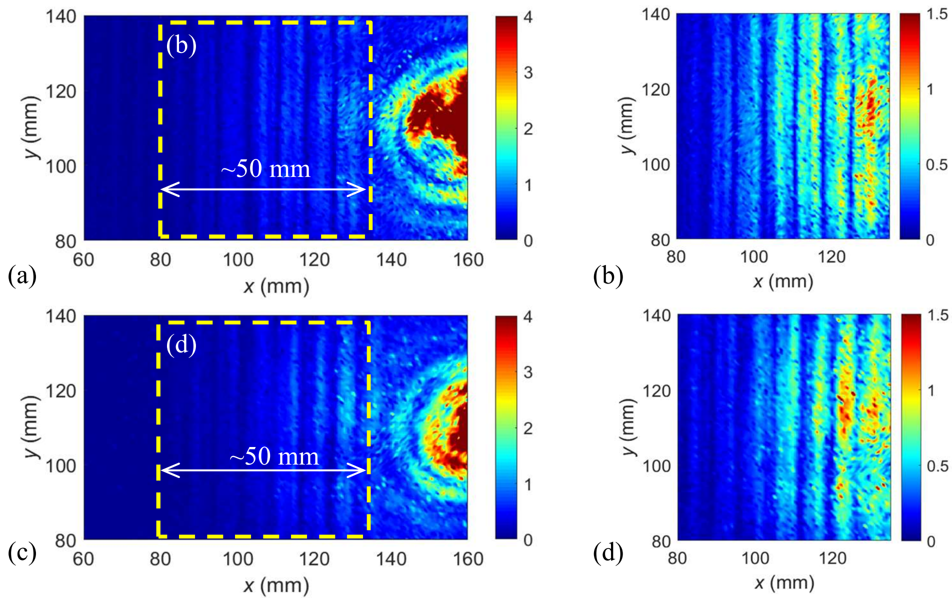

Figure 7 Wrinkle defect evaluation using adaptive wavefield imaging method. Images obtained on (a) top surface and (c) bottom surface. Zoom in images of the wrinkle defects on (b) top surface and (d) bottom surface

4. DELAMINATION INSPECTION ON A CURVED PLATE

This section presents the inspection of the curved specimen with delamination using the nonintrusive PZT-SLDV inspection system. Because the curvature of the plate affects the proper estimation of TOF when using the current PZT-SLDV experimental setup, the adaptive wavefield imaging present in Section 3 is no longer applicable. Alternatively, an imaging method based on wavenumber analysis is developed and adopted for the curved plate inspection. The wavenumber imaging algorithms and the inspection results are presented in this section.

4.1. EVALUATION METHOD: WEIGHTED WAVENUMBER IMAGING

Using multidimensional Fourier transform (FT) [37], the SLDV acquired multidimensional time-space wavefield $v(t, \mathbf{x})$ can be converted to frequency-wavenumber representation to reveal intrinsic wave characteristics related to propagation and wave-defect interactions [21, 37]. The intensity of the wavenumber presents how the Lamb waves are modified at defect due to the wave-defect interactions. Hence a wavenumber distribution map can be used to directly indicate the presence of the defect as well as its location in the structure.

In this study, a weighted wavenumber imaging method using wavenumber information at selected frequencies of interest is developed and applied for the delamination detection in the curved plate. The method first transfers the acquired time-space wavefield $v(t, \mathbf{x})$ to the frequency-space representation $V(f, \mathbf{x})$ through 1D Fourier transform w.r.t. time t, given as:

$$V(f,\mathbf{x}) = \int_{-\infty}^{\infty} v(t,\mathbf{x}) e^{-j2\pi ft} dt \tag{4}$$

After that, short-space 2D FT previously developed in [19] is applied to the frequency-space wavefield $V(f, \mathbf{x})$ w.r.t. space $\mathbf{x}$, resulting in a space-frequency-wavenumber representation $S(\bar{\mathbf{x}}, f, \mathbf{k})$, as:

$$S(\bar{\mathbf{x}}, f, \mathbf{k}) = \int_{-\infty}^{\infty}\int_{-\infty}^{\infty} V(f,\mathbf{x}) W(\mathbf{x}-\bar{\mathbf{x}}) e^{j\mathbf{k}\cdot\mathbf{x}} d\mathbf{x} \tag{5}$$

where $\bar{\mathbf{x}}$ is the retained spatial vector $(\bar{x}, \bar{y})$ for each scanning point, $\mathbf{k}$ is the counterpart of $\mathbf{x}$ in the wavenumber domain, and $W(\mathbf{x})$ is a spatial window function centered at $\bar{\mathbf{x}}$ sliding through the whole scanning area during the process of short-space 2D FT. In this study, Hanning window is used [38], given as:

$$W(\mathbf{x}) = \begin{cases} \frac{1}{2}\left[1 + \cos\left(2\pi \frac{|\mathbf{x}|}{D}\right)\right] & \text{if } |\mathbf{x}| \leq D/2 \\ 0 & \text{otherwise} \end{cases} \tag{6}$$

where D is the window width in the space domain along both x and y directions. More details of the short-space 2D FT can be referred to [19]. In order to obtain the wavenumber distribution in the scanned area, the calculated $S(\bar{\mathbf{x}}, f, \mathbf{k})$ at each scanning point $\bar{\mathbf{x}}$ is weighted by considering the contribution of each wavenumber component $|\mathbf{k}|$, resulting an effective wavenumber $k(\bar{\mathbf{x}}, f)$, which is expressed as:

$$k(\bar{\mathbf{x}}, f) = \frac{\sum_{\mathbf{k}} |S(\bar{\mathbf{x}}, f, \mathbf{k})||\mathbf{k}|}{\sum_{\mathbf{k}} |S(\bar{\mathbf{x}}, f, \mathbf{k})|} \tag{7}$$

The obtained wavenumber function $k(\bar{\mathbf{x}}, f)$ represents the wavenumber distribution within an area defined by $\bar{\mathbf{x}}$ at each frequency f. To acquire the wavenumber image at the excitation frequency with a good resolution, an image fusion technique is performed by taking the average of $k(\bar{\mathbf{x}}, f)$ over a selected frequency range about the excitation frequency, expressed as:

$$k(\bar{\mathbf{x}}) = \frac{1}{N} \sum_{i=1}^{N} k(\bar{\mathbf{x}}, f_i), \tag{8}$$

where f_i (i = 1, 2, 3… N) are the frequencies within the selected frequency band. $k(\bar{\mathbf{x}})$ is therefore the wavenumber distribution plotted as an intensity image that shows how the wavenumber changes at defect when it is present.

4.2. EVALUATION OF DELAMINATION IN THE CURVED PLATE

The curved composite plate is manufactured with embedded delamination in between different layers. The top surface and side view of the curved plate are shown in Figure 8a and Figure 8b respectively. The plate measures about 101 mm high and 7 mm thick, and 160 mm top surface arc length. Two area inspections are performed on each surface of the plate with one for the wing W1 and another for W2 as shown in Figure 8c. A 3-count toneburst amplified to 50 Vpp is used as excitation for each inspection. The excitations are located at the center of each wing, O_1 for W1 and O_2 for W2, so that the wave propagation can cover that the entire wing. Inspection frequency evaluation similar to that given in Section 3.2 is performed, and 150 kHz is selected as it provides strong wave-defect interaction. The SLDV head is placed normal to the surface where the excitation is located as shown in Figure 8d. Due to the curvature of the plate, the SLDV will not maintain normal to the plate surface of the whole scan area, as illustrated in Figure 8d. Such scanning angle effect and resulted loss in wave strength are not considered in this study since our study goal is to explore if the present measurement and analysis methods are applicable for delamination detection on plates with such amount of curvature. For each inspection, the scanning area covers the accessible surface of the inspected wing: around 90 mm × 90 mm within x-y plane. The SLDV spatial resolution is 1 mm and the sampling rate is 10.24 MHz. Note the inspection area on top and bottom surface differs subtlety due to the plate curvature.

Figure 9a and Figure 9b plot the wavefield snapshots at 45 μs for W1 and W2 inspection on the top surface. The wave-delamination interactions can be immediately noticed at two locations along y=50 mm (marked as D2) and 82 mm (marked as D1) from the wavefield plots. Similar wave-defect interactions are observed: (a) defect induced waves at D1 as shown in Figure 10d with significantly smaller wavelength compared to the 10 mm nominal wavelength of the incident waves (Figure 9c); (b) defect induced waves at D2 (Figure 9e) with obvious higher intensity while no obvious wavelength change compared to the incident waves (Figure 9e) indicating possibility of presence of defect.

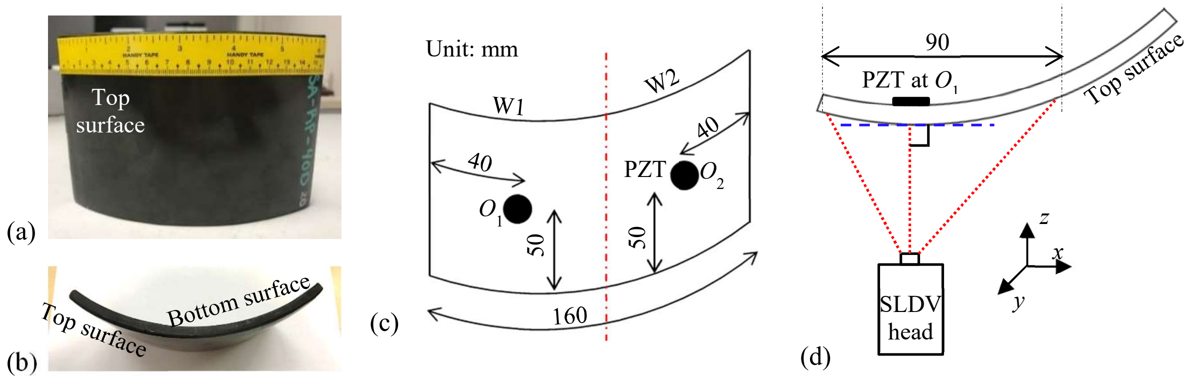

Figure 8 Inspection of curved plate with delamination (photo courtesy of NASA Langley Research Center and the ACC members): (a) top surface view, (b) side view showing the curvature, (c) actuation locations for W1 and W2 inspection, (d) actuation and sensing schematic for W1

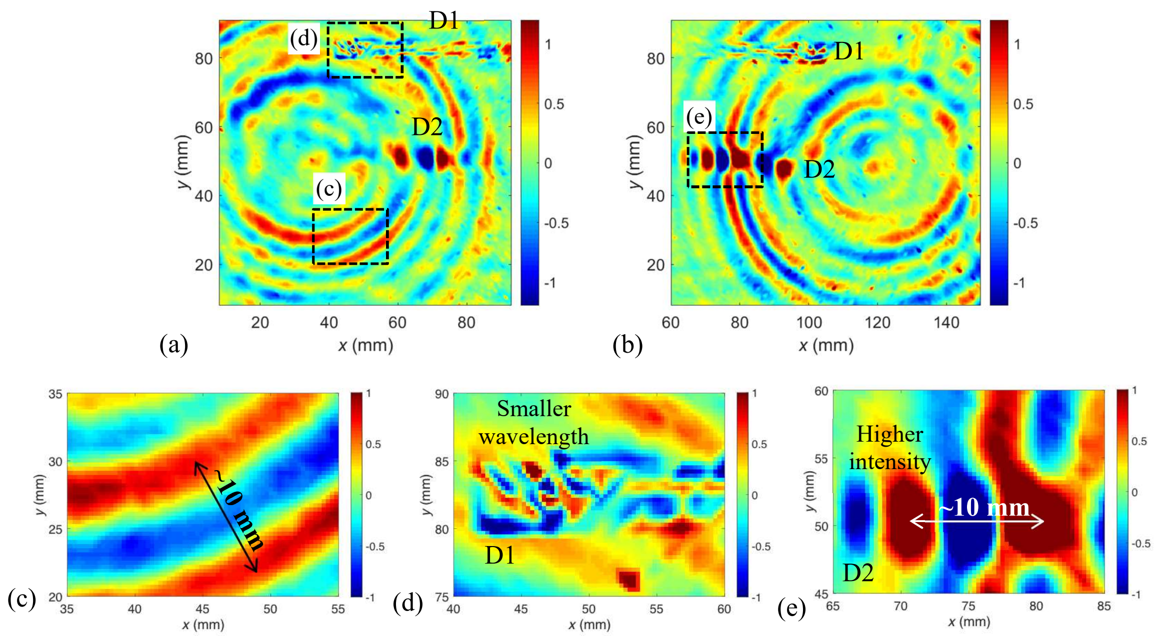

Figure 9 Wavefield result at 45 μs obtained on top surface of (a) W1, (b) W2, (c) zoom in view the wavelength of incident waves, (d) zoom in view of the smaller wavelength of the defect induced waves, and (e) zoom in view of the larger wavelength of the defect induced waves

Further evaluation of the delamination in the curved plate is conducted with the weighted wavenumber imaging method given in section 4.1. The resulted wavenumber images are plotted in Figure 10a and Figure 10b. From the image for W1 (Figure 10c), a strip shaped defect (D1) is highlighted with large wavenumbers in the range 40 mm to 90 mm along y=82 mm, which is consistent with the shorter wavelength observed in the wavefield snapshot (Figure 9d) given the inverse relationship between wavenumber and wavelength [19]. In addition, another strip like defect (D2) can also be observed in the range x=40-90 mm at y=50 mm through the indication via slightly wavenumber variations, which is consistent with the wavefield observation that no obvious wavelength change (Figure 9e). In the wavenumber image for W2 (Figure 10b), D1 (y=80 mm) and D2 (y=50 mm) are indicated in the range 60 mm to 110 mm along x axis. By comparing the imaging results of W1 and W2, we can conclude that D1 and D2 are localized in the range 40 mm to 110 mm along x axis with D1 at 82 mm and D2 at 50 mm along y axis.

The inspection wavenumber imaging results obtained on bottom surface are presented in Figure 10c and Figure 10d. Similar subtle wavenumber variation are observed at the D2 location detected earlier on the top surface, which further confirms the D2 range and shape. In addition, another strip shaped defect (D3) is observed, located at y=18 mm with similar range along x axis, 40-110 mm by considering both the results of Figure 10c and Figure 10d. Through comparing the inspection results on top and bottom surface, we can conclude that: (1) three strip shape defect exist in the plate in the range about 40 mm to 110 mm along the x axis with D1 at 82 mm, D2 at 50 mm and D3 at 18 mm along y axis, and (2) along the thickness direction, D1 is close to top surface since it is only clearly highlighted in the results obtained on the top surface, while D3 is close to the bottom surface since it is only visualized in the results measured on the bottom surface. D2 shall be located within the middle plane since the interaction is more difficult to capture on both surfaces resulting in lower imaging resolution.

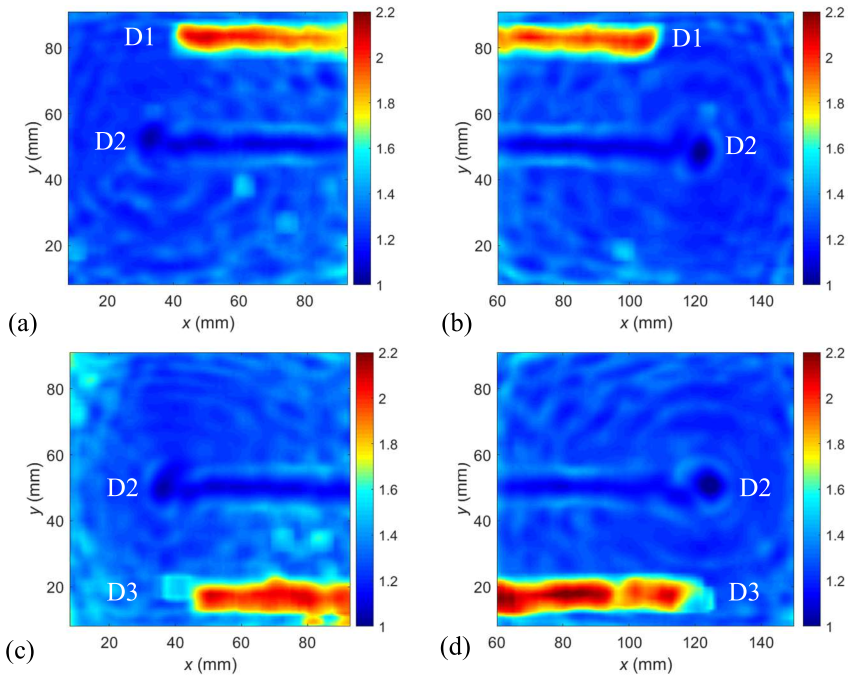

Figure 10 Wavenumber imaging results of the curved plate obtained on the top surface: (a) W1, and (b) W2; obtained on the bottom surface: (c) W1, and (d) W2

5. CONCLUSIONS

In this paper, two laminated composite plates, flat plate with wrinkle defect and curved plate with delamination, are evaluated using a nonintrusive PZT-SLDV system without detailed manufacturing information about the structures. For the wrinkle plate, the first arrival shows clear wave interactions with defect and thus is used to evaluate the wrinkles through an adaptive wavefield imaging method. The resulted images clearly present the wrinkle defect patterns as well as their location and ranges. While for evaluation of delamination in the curved plate, promising results are also obtained with the current setup. Wavelength change are observed compared to the incident waves in the time-space wavefield, indicating wavenumber changes in the wavenumber domain. Therefore, the wavenumber imaging method is employed to evaluate the delamination in the curved plate. The resulted images clearly indicate three delamination defects, including their location, overall sizes, and shapes. In addition, the defect location along the thickness direction is indicated with D1 near the top surface, D2 in the middle, and D3 close to the bottom surface.

Although both the wrinkles and delamination in the two plates are localized in the resulted images, there are still some improvements can be achieved for both plates: (1) the left edge of the wrinkle region on the wrinkle plate is not identified since most of the wave energy scattered after interacting with wrinkles as well as attenuated after propagating long distance; (2) delamination D2 is not visualized as clearly as other two delamination, and one possible reason could be that the selected excitation location is too close to the defect. Future work can be focused on trying additional actuator locations such as left and right edges of the plate to cover more inspection views and/or allow wave propagation before the defect. In addition, 3D laser vibrometer can be explored for curve plate inspection. Moreover, implementation of the PZT-SLDV system on other composite defect evaluation such as porosity is also another direction.

6. ACKNOWLEDGMENTS

The authors would like to thank the financial supports from NASA Advanced Composite Project under Award Nos. NNL09AA00A and 80LARC17C0004. The material is based upon work supported by NASA under Award Nos. NNL09AA00A and 80LARC17C0004. Any opinions, findings, and conclusions or recommendations expressed in this material are those of the author(s) and do not necessarily reflect the views of the National Aeronautics and Space Administration.

7. REFERENCES

[1] Garnier, C., Pastor, M.-L., Eyma, F., and Lorrain, B., 2011, "The detection of aeronautical defects in situ on composite structures using Non Destructive Testing," Composite structures, 93(5), pp. 1328-1336.
[2] Leckey, C. A., and Juarez, P. D., 2016, "Ultrasonic NDE Simulation for Composite Manufacturing Defects."
[3] Howell, P. A., 2020, "Nondestructive Evaluation (NDE) Methods and Capabilities Handbook-Volume II Appendices-Appendix A-Appendix D."
[4] Leckey, C. A., Seebo, J. P., and Juarez, P., 2016, "Challenges of NDE simulation tool validation, optimization, and utilization for composites," Proc. AIP Conference Proceedings, AIP Publishing, p. 120011.
[5] Bowkett, M., and Thanapalan, K., 2017, "Damage Detection and Critical Failure Prevention of Composites," Failure Analysis and Prevention, IntechOpen.
[6] Radzieński, M., Kudela, P., Marzani, A., De Marchi, L., and Ostachowicz, W., 2019, "Damage Identification in Various Types of Composite Plates Using Guided Waves Excited by a Piezoelectric Transducer and Measured by a Laser Vibrometer," Sensors, 19(9), p. 1958.
[7] Mizukami, K., Mizutani, Y., Todoroki, A., and Suzuki, Y., 2016, "Detection of in-plane and out-of-plane fiber waviness in unidirectional carbon fiber reinforced composites using eddy current testing," Composites Part B: Engineering, 86, pp. 84-94.
[8] Cramer, K. E., Leckey, C. A., Howell, P. A., Johnston, P. H., Burke, E. R., Zalameda, J. N., Winfree, W. P., and Seebo, J. P., 2015, "Quantitative NDE of Composite Structures at NASA."
[9] Victor, M., Marianne, P., Marie-Laetitia, P., Helene, W., Arthur, C., and Moussa, K., 2013, "Application of non destructive testing to the detection of aeronautical defects in composite structures," Nonconventional Technologies Review.
[10] Giurgiutiu, V., 2007, Structural health monitoring: with piezoelectric wafer active sensors, Elsevier.
[11] Yuan, F.-G., 2016, Structural health monitoring (SHM) in aerospace structures, Woodhead Publishing.
[12] Rose, J. L., 2014, Ultrasonic guided waves in solid media, Cambridge university press.
[13] Sohn, H., Dutta, D., Yang, J., DeSimio, M., Olson, S., and Swenson, E., 2011, "Automated detection of delamination and disbond from wavefield images obtained using a scanning laser vibrometer," Smart Materials and Structures, 20(4), p. 045017.
[14] Park, H. W., Sohn, H., Law, K. H., and Farrar, C. R., 2007, "Time reversal active sensing for health monitoring of a composite plate," Journal of Sound and Vibration, 302(1-2), pp. 50-66.
[15] Purekar, A., and Pines, D., 2010, "Damage detection in thin composite laminates using piezoelectric phased sensor arrays and guided Lamb wave interrogation," Journal of Intelligent Material Systems and Structures, 21(10), pp. 995-1010.
[16] Rogge, M. D., and Leckey, C. A., 2013, "Characterization of impact damage in composite laminates using guided wavefield imaging and local wavenumber domain analysis," Ultrasonics, 53(7), pp. 1217-1226.
[17] Hall, J. S., and Michaels, J. E., 2015, "Multipath ultrasonic guided wave imaging in complex structures," Structural Health Monitoring, 14(4), pp. 345-358.
[18] Sohn, H., Dutta, D., Yang, J.-Y., Park, H.-J., DeSimio, M., Olson, S., and Swenson, E., 2011, "Delamination detection in composites through guided wave field image processing," Composites science and technology, 71(9), pp. 1250-1256.

[19] Tian, Z., Yu, L., and Leckey, C., 2015, "Delamination detection and quantification on laminated composite structures with Lamb waves and wavenumber analysis," Journal of Intelligent Material Systems and Structures, 26(13), pp. 1723-1738.
[20] Staszewski, W., Lee, B., and Traynor, R., 2007, "Fatigue crack detection in metallic structures with Lamb waves and 3D laser vibrometry," Measurement Science and Technology, 18(3), p. 727.
[21] Michaels, T. E., Michaels, J. E., and Ruzzene, M., 2011, "Frequency–wavenumber domain analysis of guided wavefields," Ultrasonics, 51(4), pp. 452-466.
[22] Yu, L., and Tian, Z., 2013, "Lamb wave structural health monitoring using a hybrid PZT-laser vibrometer approach," Structural Health Monitoring, 12(5-6), pp. 469-483.
[23] Kudela, P., Radzieński, M., and Ostachowicz, W., 2015, "Identification of cracks in thin-walled structures by means of wavenumber filtering," Mechanical Systems and Signal Processing, 50, pp. 456-466.
[24] Flynn, E. B., Chong, S. Y., Jarmer, G. J., and Lee, J.-R., 2013, "Structural imaging through local wavenumber estimation of guided waves," Ndt & E International, 59, pp. 1-10.
[25] Tian, Z., Yu, L., Leckey, C., and Seebo, J., 2015, "Guided wave imaging for detection and evaluation of impact-induced delamination in composites," Smart Materials and Structures, 24(10), p. 105019.
[26] Mesnil, O., Leckey, C. A., and Ruzzene, M., 2015, "Instantaneous and local wavenumber estimations for damage quantification in composites," Structural Health Monitoring, 14(3), pp. 193-204.
[27] Ostachowicz, W., Radzieński, M., and Kudela, P., 2014, "50th anniversary article: comparison studies of full wavefield signal processing for crack detection," Strain, 50(4), pp. 275-291.
[28] Juarez, P. D., and Leckey, C. A., 2015, "Multi-frequency local wavenumber analysis and ply correlation of delamination damage," Ultrasonics, 62, pp. 56-65.
[29] Yu, L., Tian, Z., Li, X., Zhu, R., and Huang, G., 2019, "Core–skin debonding detection in honeycomb sandwich structures through guided wave wavefield analysis," Journal of Intelligent Material Systems and Structures, 30(9), pp. 1306-1317.
[30] Yu, L., Tian, Z., and Leckey, C. A., 2015, "Crack imaging and quantification in aluminum plates with guided wave wavenumber analysis methods," Ultrasonics, 62, pp. 203-212.
[31] Leong, W., Staszewski, W., Lee, B., and Scarpa, F., 2005, "Structural health monitoring using scanning laser vibrometry: III. Lamb waves for fatigue crack detection," Smart Materials and Structures, 14(6), p. 1387.
[32] Ruzzene, M., Jeong, S., Michaels, T., Michaels, J., and Mi, B., "Simulation and measurement of ultrasonic waves in elastic plates using laser vibrometry," Proc. AIP Conference Proceedings, AIP, pp. 172-179.
[33] Michaels, J. E., 2017, "Ultrasonic wavefield imaging: Research tool or emerging NDE method?."
[34] Giurgiutiu, V., 2005, "Tuned Lamb wave excitation and detection with piezoelectric wafer active sensors for structural health monitoring," Journal of intelligent material systems and structures, 16(4), pp. 291-305.
[35] Stepanishen, P. R., and Benjamin, K. C., 1982, "Forward and backward projection of acoustic fields using FFT methods," The Journal of the Acoustical Society of America, 71(4), pp. 803-812.
[36] Tian, Z., Howden, S., Ma, Z., Xiao, W., and Yu, L., 2019, "Pulsed laser-scanning laser Doppler vibrometer (PL-SLDV) phased arrays for damage detection in aluminum plates," Mechanical Systems and Signal Processing, 121, pp. 158-170.
[37] Ruzzene, M., 2007, "Frequency-wavenumber domain filtering for improved damage visualization," Ultrasonic And Advanced Methods For Nondestructive Testing And Material Characterization, World Scientific, pp. 591-611.
[38] Tian, Z., and Yu, L., 2014, "Lamb wave frequency–wavenumber analysis and decomposition," Journal of Intelligent Material Systems and Structures, 25(9), pp. 1107-1123.